Contents lists available at ScienceDirect

Acta Astronautica

Numerical exploration of mixing and combustion in ethylene fueled scramjet combustor

CrossMark

Malsur Dharavath, P. Manna, Debasis Chakraborty [1]

Directorate of Computational Dynamics, Defence Research and Development Laboratory, Kanchanbagh, Hyderabad 500058, India

A R T I C L E   I N F O

A B S T R A C T

Numerical simulations are performed for full scale scramjet combustor of a hypersonic airbreathing vehicle with ethylene fuel at ground test conditions corresponding to flight Mach number, altitude and stagnation enthalpy of 6.0, 30 km and 1.61 MJ/kg respectively. Three dimensional RANS equations are solved along with species transport equations and *SST-kω* turbulence model using Commercial CFD software *CFX*-11. Both nonreacting (with fuel injection) and reacting flow simulations [using a single step global reaction of ethylene-air with combined combustion model (CCM)] are carried out. The computational methodology is first validated against experimental results available in the literature and the performance parameters of full scale combustor in terms of thrust, combustion efficiency and total pressure loss are estimated from the simulation results. Parametric studies are conducted to study the effect of fuel equivalence ratio on the mixing and combustion behavior of the combustor.

1. Introduction

The applications of hypersonic propulsion include high-speed transport, national defense, space access etc. Scramjet engine is the preferred choice for hypersonic air-breathing cruise vehicle. Research of scramjet engines started way back in the 1960s, but the flight testing of scramjet-powered airbreathing mission is attempted in the last decade. Many technical issues need to be addressed before scramjet engines are used in any practical vehicle. Different fuel injection systems namely struts, pylons or cavities [1] are used for scramjet engine. Injection, mixing and burning of fuel within the combustor length are some of the major challenges in the realization of a flight worthy scramjet combustor. For volume limited applications and for $M_\infty < 8$, hydrocarbon fuel has many

advantages and number of experimental and numerical studies of scramjet combustor with hydrocarbon fuel has appeared in the recent literature. Gruenig and Mayinger [2] studied the performance of pylon injected liquid hydrocarbon supersonic combustor experimentally and found that gas dynamic feedback mechanism strongly affects the supersonic combustion process for kerosene fuel. Hu et al. [3] studied the performance of scramjet combustor with kerosene fuel injected from strut and wall mounted injector at equivalence ratio with different proportions and observed that combustion characteristics vary significantly with the strut/wall fuel feeding ratio, especially when this ratio is close to its lowest and highest limits. Zhang et al. [4] carried out experimental investigation of a strut based hydrocarbon fueled scramjet combustor and studied three different combustion mode (scramjet mode, weak ramjet mode and strong ramjet mode) transitions with respect to fuel equivalence ratio. The nonlinear characteristics of wall-pressures near the exit of the isolator were used to detect different

E-mail address: debasis_cfd@drdl.drdo.in (D. Chakraborty).
[1] Tel.: +91 40 24583310; fax: +91 40 24340037.

Notation

A	pre-exponent factor [$m^{2.25}/mol^{0.75}$ s] and area [m^2]
CCM	Combined Combustion Model
E	activation energy [J/kg]
EDM	Eddy Dissipation Model
F	momentum [N]
FRCM	Finite Rate Chemistry model
GCI	Grid Convergence Index
h	combustor height at entry, 1st grid spacing
H	enthalpy [J/kg]
I	species component
M	Mach number
P	pressure [N/m^2]
$\dot{w}$	reaction rate [kmol/m^3]
RANS	Reynolds Averaged Navier Stokes
S	source term
SST	Shear Stress Transport
X	combustor length along the flow direction [m]
Y	combustor height [m] and Mass fraction
Z	combustor width [m]
h	height of the combustor entry [m]
k	turbulent kinetic energy [J/kg]
q	heat flux [W/m^2]
t	time [s]
u	velocity [m/s]

Symbol

δ	temperature exponent
ω	turbulent frequency rate [1/s]
μ	dynamic viscosity [N/m^2 s]
ρ	density [kg/m^3]
τ	shear stress [N/m^2 s]
ϕ	equivalence ratio
η	efficiency
∞	free stream condition
Pr	Prandtl number
σ	constant value of k, ε and ω terms
ν	stiochiometric coefficient
χ	molar concentration

Subscript

CI	combustor inlet
c	coefficient
i,j,k	in x,y,z coordinate directions
inj	injection location
k	elementary reaction
l	laminar
t	turbulent

combustion modes. Fan et al. [5] studied the effect of entry static pressure, entry Mach number, combustor entry geometry, and injection scheme on combustor performance with thermally cracked kerosene and observed higher combustor entry Mach number as well as a larger combustor duct height suppress the boundary layer separation near the combustor entrance and avoid the problem of inlet un-start. Yu et al. [6,7] compared the performance of several cavity based kerosene fueled scramjet combustor and spray structures with pure liquid and effervescent atomization. Combustion efficiency with effervescent atomization is found to be 15–20% more compared to pure liquid atomization. Cavity configuration with combined open–closed cavities was demonstrated to have better combustion performance than a single-cavity module.

Vapourisation, mixing and combustion of a kerosene fueled scramjet combustor using struts are studied in detail [8] to deliver the required thrust for a hypersonic flight vehicle. Dharavath et al. [9] performed end to end simulation of scramjet integrated hypersonic cruise vehicle using three dimensional nonreacting simulation of vehicle forebody, intake and tail region and reacting flow simulation in the scramjet combustor. Positive thrust minus drag for the operating altitude of 31.0 km and Mach number 6.0 was demonstrated and the numerical simulation formed the basis of vehicle performance calculation.

Among other hydrocarbon fuels, ethylene provides an attractive option for scramjet engine due to its simpler chemical structure, gaseous injection, better mixing and ignition capabilities. The experimental results of Zhong et al. [10] showed that ethylene had higher static pressure level, specific impulse and combustion efficiency compared to vaporized kerosene for its higher activity. The difference of combustion performance between vaporized kerosene and ethylene was narrowed with the increase of equivalence ratio. Reynolds Averaged Navier–Stokes calculations were carried out [11] for a dual mode scramjet in the M_∞ range of 4.0–6.5 with gaseous ethylene fuel injection from wall-mounted injection ports and a recessed cavity for flame holding. The combustor was operated for both $M_\infty = 4.0$ and 6.5 conditions in dual mode. Thermal choking of the flow was not observed at Mach 6.5 condition. It was reported that the solutions for dual-mode operation were very sensitive to turbulence model and turbulent Prandtl and Schmidt numbers. An integrated theoretical/numerical investigation [12] for mixing in a cavity based ethylene fueled scramjet combustor was carried out to establish the ignition by air throttling downstream of the flame holder. Increase in air stream temperature and pressure and decrease in flow velocity led to smooth and reliable ignition [12]. Numerical studies were carried out in Mach 2 flow with in-stream ethylene fuel injection through pylons and the performances were predicted for various pylon configurations [13]. The effects of ethylene fuel injection in airflow are experimentally studied in a cavity based flameholder in a supersonic flow [14]. It is shown that cavity based fuel injection and flame-holding offer an obstruction-free flow path in hydrocarbon fueled scramjet engines. Tam et al.

[15] performed numerical studies for gaseous ethylene fuel/air mixing characteristics with several strut fuel-injection schemes in Mach 2 inflow condition in a rectangular flow path and proposed optimum strut design.

It is clear that ethylene fueled scramjet combustor has not been investigated very rigorously compared to hydrogen or kerosene fueled scramjet. An ethylene fueled scramjet combustor is being developed to demonstrate autonomous functioning of vehicle integrated scramjet engine for hypersonic airbreathing cruise mission [16]. To supply fuel appropriately in the combustor, a strut based injection system is considered. Both numerical and experimental studies are performed to realize the flight sized scramjet combustor with ethylene fuel. Since, ground testing is expensive and making measurements of the flow within a supersonic combustion chamber is very difficult, accurate numerical simulations of the injection, mixing and combustion process in supersonic flow can guide the experimental work.

In the present work, three-dimensional reacting simulations are presented for scramjet combustor with ethylene fuel. The computational methodology is first validated for experimental results of gaseous ethylene fueled cavity based model scramjet combustor. The validated methodology is then applied to analyze a flight sized scramjet combustor with ethylene fuel injected from a row of struts placed in the flow path for the ground test condition. Flow variables are analyzed both for nonreacting (cold flow) and reacting flow conditions. The net engine performance in terms of mixing (nonreacting flow with fuel), combustion efficiencies, and thrust is evaluated from simulation results. Parametric studies are also carried out to investigate the effect of fuel equivalence ratio on mixing and combustion characteristics of the scramjet combustor.

2. Computational methodology

Three-dimensional Reynolds Averaged Navier Stokes (RANS) equations along with species and turbulence transport equations are solved using commercial CFD code *CFX* [17]. The code is fully implicit, finite volume method with finite element based discretization of geometry capable of solving diverse and complex multidimensional fluid flow problems. The convective terms are discretized by first order upwind difference scheme till few time steps initially and subsequently, 2nd order spatial scheme is employed to capture the flow features more accurately. Menter's shear stress transport, *SST-kω* [18] turbulence model which takes both the advantages of standard *k-ε* model (for shear flows) and Wilcox's *k-ω* model (for wall turbulence) was used along with wall functions in the present simulation.

2.1. Governing equations

The system of governing equations describing the conservation of mass, momentum, energy and species transport equations of compressible gas flows are written as

Conservation of Mass equation:

$$\frac{\partial \rho}{\partial t} + \frac{\partial}{\partial x_k}(\rho\, u_k) = 0 \quad k = 1, 2, 3 \tag{1}$$

Conservation of Momentum equation:

$$\frac{\partial}{\partial t}(\rho\, u_i) + \frac{\partial}{\partial x_k}(\rho\, u_i\, u_k) + \frac{\partial P}{\partial x_i} = \frac{\partial(\tau_{ik})}{\partial x_k}, \quad i, k = 1, 2, 3 \tag{2}$$

Conservation of Energy equation:

$$\frac{\partial}{\partial t}(\rho\, H) + \frac{\partial}{\partial x_k}(\rho\, u_k H) = -\frac{\partial}{\partial x_k}(u_j\, \tau_{jk}) + \frac{\partial q_k}{\partial x_k},$$
$$j, k = 1, 2, 3 \tag{3}$$

2.2. Turbulence transport equations

2.2.1. k-ε turbulence model
Turbulent kinetic energy (k) equation:

$$\frac{\partial}{\partial t}(\rho\, k) + \frac{\partial}{\partial x_k}(\rho\, u_k k) = \frac{\partial}{\partial x_k}\left(\left(\frac{\mu_l}{Pr} + \frac{\mu_t}{\sigma_k}\right)\frac{\partial k}{\partial x_k}\right) + S_k \tag{4}$$

Turbulent eddy dissipation (ε) equation:

$$\frac{\partial}{\partial t}(\rho\, \varepsilon) + \frac{\partial}{\partial x_k}(\rho\, u_k \varepsilon) = \frac{\partial}{\partial x_k}\left(\left(\frac{\mu_l}{Pr} + \frac{\mu_t}{\sigma_\varepsilon}\right)\frac{\partial \varepsilon}{\partial x_k}\right) + S_\varepsilon \tag{5}$$

where ρ, u_i, p, H are the density, velocity components, pressure and total energy respectively and $\mu = \mu_l + \mu_t$ is the total viscosity; μ_l, μ_t being the laminar and turbulent viscosity and Pr is the Prandtl number. The source terms S_k and S_e of the k and ε equation are defined as

$$S_K = \tau_{ik}\frac{\partial u_i}{\partial x_k} - \rho\, \varepsilon \quad \text{and} \quad S_\varepsilon = C_{\varepsilon 1}\tau_{ik}\frac{\partial u_i}{\partial x_k} - C_{\varepsilon 2}\frac{\rho\, \varepsilon^2}{k}$$

where turbulent shear stress is defined as

$$\tau_{ik} = \mu_t\left(\frac{\partial u_i}{\partial x_k} + \frac{\partial u_k}{\partial x_i}\right) \tag{6}$$

Laminar viscosity (μ_l) is calculated from Sutherland law as

$$\mu_l = \mu_{ref}\left(\frac{T}{T_{ref}}\right)^{3/2}\left(\frac{T_{ref} + S}{T + S}\right) \tag{7}$$

where T is the temperature and μ_{ref}, T_{ref} and S are known coefficient. The turbulent viscosity μ_t is calculated as

$$\mu_t = C_\mu\frac{\rho\, k^2}{\varepsilon} \tag{8}$$

The coefficients involved in the calculation of turbulent viscosity (μ_t) are taken as

$$C_\mu = 0.09, \quad C_{\varepsilon 1} = 1.44, \quad C_{\varepsilon 2} = 1.92$$
$$\sigma_K = 1.0, \quad \sigma_\varepsilon = 1.3, \quad \sigma_c = 0.9$$

The heat flux q_k is calculated as $q_k = -\lambda(\partial T/\partial x_k)$, λ is the thermal conductivity

2.2.2. k-ω turbulence model
In this model, turbulent viscosity is calculated as function of k and ω

$$\mu_t = f\left(\frac{\rho k}{\omega}\right) \tag{9}$$

Turbulent kinetic energy (k) equation:

$$\frac{\partial}{\partial t}(\rho k) + \frac{\partial}{\partial x_i}(\rho k u_i) = \frac{\partial}{\partial x_j}\left(\Gamma_k \frac{\partial k}{\partial x_j}\right) + G_k - Y_k \tag{10}$$

Specific dissipation rate (ω) equation:

$$\frac{\partial}{\partial t}(\rho\omega) + \frac{\partial}{\partial x_i}(\rho\omega u_i) = \frac{\partial}{\partial x_j}\left(\Gamma_\omega \frac{\partial \omega}{\partial x_j}\right) + G_\omega - Y_\omega \tag{11}$$

where G_k is turbulence production due to viscous and buoyancy forces, $Y_k = \beta^1 \rho k w$, $\Gamma_k = \mu + (\mu_t/\sigma_k)$, $G_w = \alpha(\omega/k)G_K$, $Y_w = \beta\rho w^2$ and $\Gamma_w = \mu + (\mu_t/\sigma_w)$ of the k and ω equations respectively, where $\beta^1 = 0.09$, $\alpha = 5/9$, $\beta = 0.075$, and $\sigma_k = \sigma_w = 2$.

2.2.3. SST- kω turbulence model

To retain the robust and accurate formulation of Wilcox's k-ω model in the near wall region, and take advantage of the free stream independence of the k-ε model in the outer part of the boundary layer, Menter [18] blended both the models through a switching function. k-ε model was transformed into Wilcox's k-ω formulation and was multiplied by $(1-F_1)$ and added to original k-ω model multiplied by F_1. The blending function F_1 will be one in the near wall region and zero away from the surface. In the second step, the definition of eddy viscosity (μ_t) was modified in the following way to account for the transport of the principal turbulent shear stress ($\tau = \overline{-\rho u'v'}$)

$$\nu_t = \frac{a_1 k}{\max(a_1\omega; \ \Omega F_2)} \tag{12}$$

where ν_t (is kinematic viscosity)$=\mu_{t/\rho}$ and F_2 is a blending function similar to F_1, which restricts the limiter to the wall boundary layer. Ω is an invariant measure of the strain rate. Their formulation is based on the distance to the nearest surface and on the flow variables:

$$F_2 = \tanh(\text{arg}_2^4) \tag{13}$$

The argument is defined as

$$\text{arg}_2 = \min\left[\max\left\{\frac{\sqrt{k}}{0.09\omega y}, \ \frac{500\nu}{y^2\omega}\right\}, \ \frac{4\rho\sigma_{\omega 2}k}{y^2\text{CD}_{k\omega}}\right] \tag{14}$$

where y is the distance to the wall and $\text{CD}_{k\omega}$ the positive portion of the cross-diffusion terms expressed as

$$\text{CD}_{k\omega} = \max\left[2\ \rho\sigma_{\omega 2}\frac{1}{\omega}\frac{\partial k}{\partial x_j}\frac{\partial \omega}{\partial x_j}, \ 10^{-20}\right] \tag{15}$$

where y is the distance to the nearest wall and ν is the kinematic viscosity.

2.3. Species transport equation

Conservation of species mass fraction (Y_I):

$$\frac{\partial}{\partial t}(\rho\ Y_I) + \frac{\partial}{\partial x_k}(\rho\ u_k Y_I) = \frac{\partial}{\partial x_k}\left[\left(\frac{\mu_I}{Pr} + \frac{\mu_t}{\sigma_c}\right)\frac{\partial Y_I}{\partial x_k}\right] + S_I \tag{16}$$

where the source term S_I is due to the chemical reaction rate involving species component I, and Y_I is the mass fraction of Ith species. The chemical reactions can be described in terms of k elementary reactions involving N_c components that can be written as

$$\sum_{I=A,B,C,\dots}^{N_c} \nu_{kI}^i I \Leftrightarrow \sum_{I=A,B,C,\dots}^{N_c} \nu_{kI}^{ii} I \tag{17}$$

where ν_{kI} is the stoichiometric coefficient for species component I in the elementary reaction k. The rate of production/consumption, S_I, for species component I can be computed as the sum of the rate of progress for all the elementary reactions in which component I participates:

$$S_I = M_{wI} \sum_{k=1}^k (\nu_{kI}^{ii} - \nu_{kI}^i)\dot{w}_k \tag{18}$$

where $M_{w\,I}$ is molecular weight of species component I and $\dot{w}_k$ is the elementary reaction rate of progress for reaction, which can be calculated using combined combustion model.

2.4. Combustion model

Present simulation uses single-step global kinetics scheme based Combined Combustion Model (CCM) which computes the minimum of the Eddy Dissipation and Finite Rate Chemistry models (i.e., ED/FRC model) reaction rate. The scheme for ethylene-oxidation involves the following one step reaction and five species:

$$\begin{aligned}C_2H_4 &+ 3(O_2 + 0.631H_2O + 2.661N_2) \\ &\to 2CO_2 + 3.841H_2O + 7.983N_2\end{aligned} \tag{19}$$
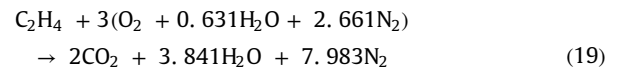
The effect of turbulent mixing on combustion is taken into account by means of the eddy-dissipation model (EDM) proposed by Magnussen and Hjertager [19] where the chemical reaction is considered fast relative to the transport process in the flow. It assumes that the reaction rate is directly proportional to the time required to mix reactants at molecular level i.e., reaction rate $\alpha\ \varepsilon/k$, where k is the turbulent kinetic energy and ε is its rate of dissipation. The reaction rate associated with turbulent mixing, is given by the minimum of the following three rates:

$$\dot{w}_{C_2H_4,\,edm} = -A_{edm}\frac{\varepsilon}{K}\min\left\{[\chi_{C_2H_4}], \frac{1}{\nu}*[\chi_{O_2}], B_{edm}*\frac{1}{1+\nu}*[\chi_p]\right\} \tag{20}$$

where $[\chi_{C_2H_4}]$, $[\chi_{O_2}]$, and $[\chi_p]$ represent the molar concentrations of the fuel, oxygen, and product species, respectively, A_{edm} and B_{edm} are empirical constants taken to be 4.0 and 0.5, respectively, ε/k the fluctuation frequency, and ν the stoichiometric oxygen to fuel mass ratio.

In FRC model, the kinetic rate of change of any species is described by Arrhenius expression. The rate of reaction

of $\dot{w}_{C_2H_4, frc}$ (in kmol/m^3 s) is given by the expression [20]

$$\dot{w}_{C_2H_4,frc} = -A_1 T^\delta \exp\left(\frac{-E_a}{R_u T}\right)[\chi_{C_2H_4}]^{0.1}[\chi_{O_2}]^{1.65}[\chi_{H_2O}]^{0.0} \quad (21)$$

The pre-exponential factor (A_1), temperature exponent (δ) and activation energy (E_a) are taken as $3.8e+12$ (kmol/cm^3)$^{-0.75}$/s, 0.0 and 30 kcal/mol respectively for present simulation. The reaction rate is determined from the minimum of the mixing and kinetic net rate by CCM and is expressed as

$$\dot{w}_{C_2H_4, combined} = \min\left[\dot{w}_{C_2H_4, edm}, \dot{w}_{C_2H_4,frc}\right] \quad (22)$$

3. Validation study

Since, various empirical constants in the turbulence models, combustion models and other transport properties are used in RANS methodology, it is necessary to validate the computational tools for similar class of problems before employing it in the design exercise. The scramjet experiment of Xiao et al. [21] with clean airstream with electric resistance heaters, cavity based flame holder and ethylene fuel is taken as the test case for validation. The schematic of the combustor alongwith the cavity based flameholder is shown in Fig. 1. The total length of the combustor is 770 mm with an isolator of 180 mm. Top wall diverges with 2° angle after a constant area section. An open cavity ($L/D \sim 4.3$) flameholder with 45° trailing edge is placed at 60 mm location from the combustor entry. Gaseous ethylene fuel with total temperature 300 K is injected transversely at sonic condition from 0.8 mm flush mounted injector orifice (5 nos) placed at the cavity bottom wall. Different fuel equivalence ratios and injection locations are considered for stabilizing the ethylene flame. The stagnation temperature, stagnation pressure, and mass flow rate of the air stream at the inlet of the combustor are 950 K, 1.0 bar and 0.73 kg/s which corresponds free stream Mach number 4.0. Static pressures at the top and bottom walls are measured in the combustor. Further details of the test conditions are available in Ref. [21].

A good quality multiblock structured grid consisting of 2.3 million grids are generated in the computational domain. Typical grid distribution in the combustor is shown in Fig. 2. Although a formal grid independence study was not carried out in the present case, but based on our earlier experience of hydrocarbon–air simulation in scramjet combustor [22,23], the grid is fine enough to capture all the essential features of the flow.

As the inflow boundary is supersonic, the flow variables at the combustor entry are kept fixed and supersonic outlet boundary condition are provided at the combustor exit. No slip and adiabatic conditions are imposed on the combustor walls. Gaseous ethylene at sonic condition with total temperature and pressure 300 K and 24.7 bar respectively is injected transversely from the injector orifice. The fuel equivalence ratio for the present simulation is 0.465. Maximum residual ($= \phi_j^{n+1} - f(\phi_j^{n+1}, \phi_j^n)) < 10^{-4}$ is taken as convergence criteria.

The computed surface pressures at the bottom wall for the nonreacting and reacting cases are compared with the experimental results [21] in Fig. 3. A very good match between the two is obtained. The computed combustion efficiency and total pressure loss for the reacting case are 89% and 53% respectively.

4. Simulation of full scale Scramjet combustor with ethylene fuel

4.1. Geometry, computational grid and boundary details

Paneerselvam et al. [16] explained a typical cruise hypersonic air-breathing mission for the demonstration of 20 s duration flight. To test the scramjet engine at ground, a vitiated air heater was used to obtain high enthalpy airflow for equivalent flight condition of total temperature and total enthalpy of 1650–1750 K and 1.55–1.65 MJ/kg respectively. Schematic diagram of the scramjet combustor and a part of the facility nozzle is shown in Fig. 4a. The combustor dimensions were non-dimensionalised with combustor entry height (h). The length of the facility nozzle and combustor is 5h and 22h respectively while width of the combustor including facility nozzle is 6h throughout the length. A middle wall with a thickness of 0.2h is placed at a distance of 3h downstream from combustor entry in the middle of the combustor which makes
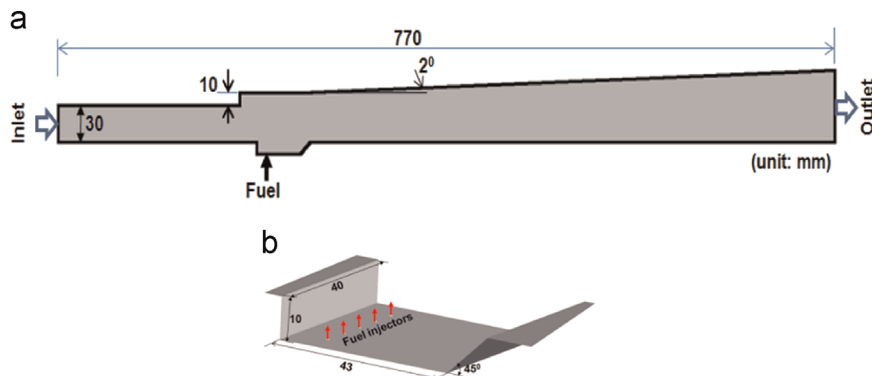

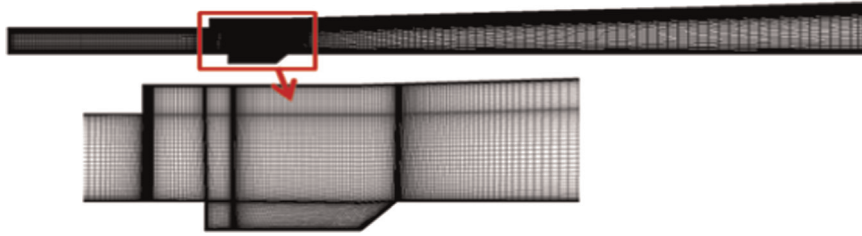**Fig. 1.** The schematic of (a) combustor geometry and (b) cavity flame holder.

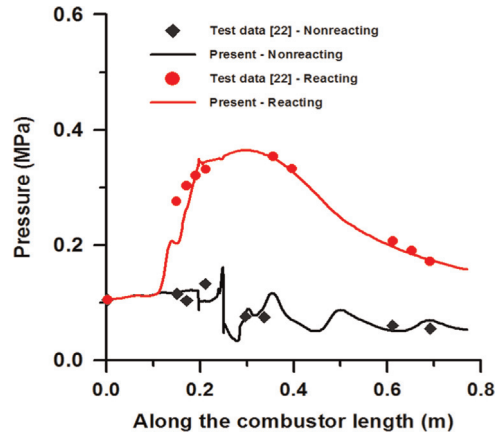**Fig. 2.** Grid distribution in the computational domain.

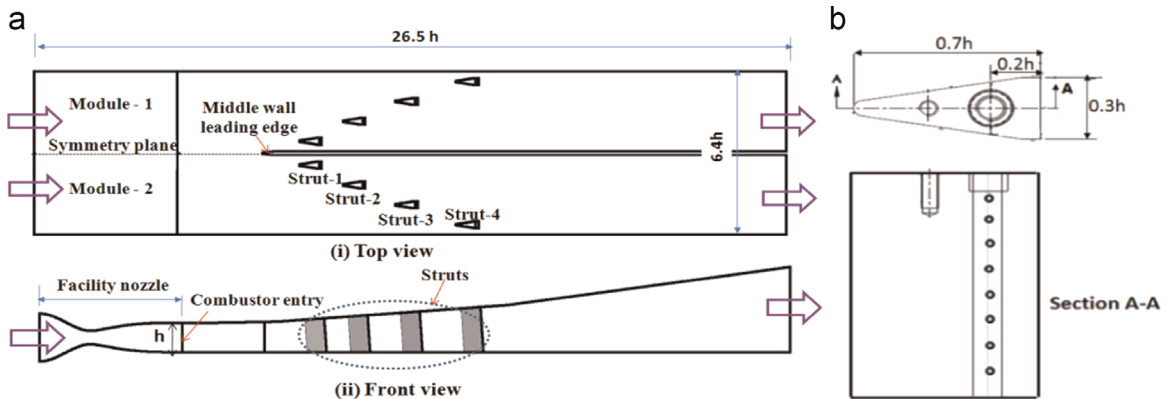**Fig. 3.** Comparison of bottom wall surface pressure for nonreacting and reacting cases.

Fig. 4. (a) Scramjet combustor with facility nozzle and (b) schematic picture of strut.

combustor into two modules. Four struts are provided in each module in such a manner that one module is the mirror image of the other about the middle wall. The struts are straight and cross section remains constant along the height of the combustor as shown in Fig. 4b. Taking the advantage of the symmetry of the geometry, only half of the geometry (i.e. Module-2 as shown in Fig. 4a) along the width of the combustor is chosen for numerical simulations to reduce the computational time. In the simulation, X-axis is taken along the flow direction (length of combustor), while, Y and Z-axes are chosen along the height and width of the combustor respectively, with the origin

being placed at the intersect point between symmetry and bottom wall at combustor entry.

Multi-block structured ($\sim$3950 block) good quality hexahedral grids with proper skewness and aspect ratio are made using *ICEM-CFD* [24] for the entire computational domain. The total grid distribution about 4.7 million points (i.e., $475 \times 95 \times 105$ grid points along the length, height and width of the combustor respectively) is generated for the computational domain of half geometry. The grids are fine near the throat and exit region of the facility nozzle, leading edges of the struts and middle wall, trailing edge regions of the struts, near-wall regions and fuel injection regions ($y^+ \sim 5$), while relatively coarser grids are provided in the remaining portion

of the nozzle and combustor. This helps to resolve the boundary layers well in the present simulations. Since, injected fuel (C_2H_4) is in the gaseous form, resolution of grids at injection holes (with size of 1.0 mm diameter) is very much necessary. A grid distribution of 8×8 is provided at each injection location to capture the area of fuel injection. Typical grid distribution on various planes and injection holes is shown in Fig. 5.

4.2. Initial and boundary conditions

Simulations are carried out for connected pipe mode test which corresponds to flight Mach number, altitude and stagnation enthalpy of 6.0, 30 km and 1.61 MJ/kg respectively. The vitiated air properties at the inflow plane and the fuel properties in the injector are tabulated in Table 1.

The vitiated air is generated by burning hydrogen and oxygen in a heater. The total temperature and pressure of the air stream are 6.24 bar and 1537 K and contain 23.3% oxygen, 62% nitrogen and 14.7% water vapor mass fractions. Gaseous ethylene fuel with total pressure and temperature of 22.9 bar and 300 K is injected transversely from the struts to the supersonic vitiated air with equivalence ratio of 0.72.

As the inflow boundary is subsonic, total temperature and total pressure are prescribed at the inflow plane. No slip and adiabatic wall boundary conditions are imposed on the walls. Symmetry boundary condition is imposed at the symmetry plane. The supersonic outflow boundary condition is applied at the exit of the computational domain. The same convergence criteria as in the validation case namely, maximum

residual ($= \phi_j^{n+1} - f(\phi_j^{n+1}, \phi_j^n)) < 10^{-4}$ is also considered here.

4.3. Simulation results

In the present work, numerical simulations of nonreacting flow with fuel injection and reacting flow with combustion are carried out to study mixing and combustion flow behavior inside combustor with ethylene fuel for an equivalence ratio of 0.72.

4.3.1. Nonreacting flow with fuel injection – mixing characterization

Ethylene fuel is injected from struts transversely into supersonic vitiated air flow. Static pressure and Mach number distribution at mid-height of combustor entry plane (i.e. $Y/h=0.5$) are shown in Fig. 6. Simulations captured all the essential features of the flow including three-dimensional effects of flow behavior inside the combustor. The various shock interactions between middle wall, struts and side walls are clearly seen in the static pressure distribution [Fig. 6(a)]. The local subsonic regions are observed [as shown in Fig. 6(b)] behind the struts and adjacent to the middle wall regions due to wake of struts and interaction of shocks and boundary layer adjacent to the middle wall regions respectively.

Static pressure distribution at different axial locations ($X/h= -4.9$, 0.0, 2.9, 5.8, 8.7, 11.6, 14.5, 17.4 and 21.5, which are represented as plane $P1$ to $P9$ respectively) is shown in Fig. 7 (a), while shock–shock interactions between middle wall, struts and side walls are shown in Fig. 7(b). Oblique shocks [$S1$ and $S2$ as shown in Fig. 7(b)] are generated due to middle
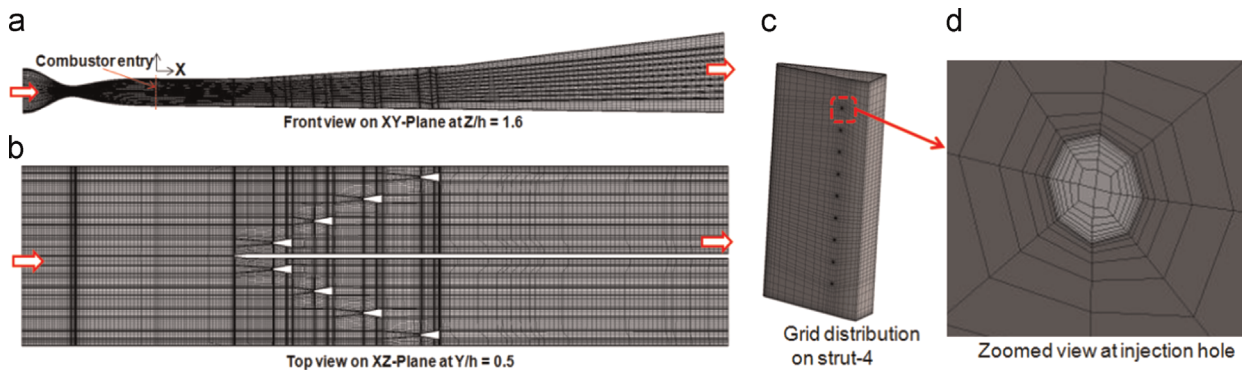

Fig. 5. Grid distribution (total grid points $\sim$4.7 millions) on various planes.

Table 1
Flow properties at the inflow plane.

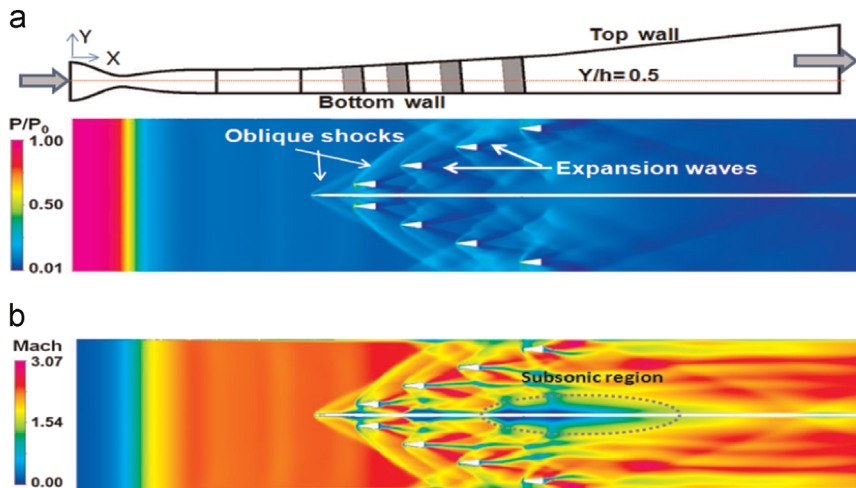| Parameter	Inflow conditions	
	Nozzle entry	Fuel injector
P_0 (bar)	6.24	22.9
T_0 (K)	1537	300
γ	1.286	1.24
Y_{O_2}	0.233	0
Y_{N_2}	0.620	0
Y_{H_2O}	0.147	0
$Y_{C_2H_4}$	0	1

Fig. 6. Distributions of (a) pressure and (b) Mach number at $Y/h=0.5$.
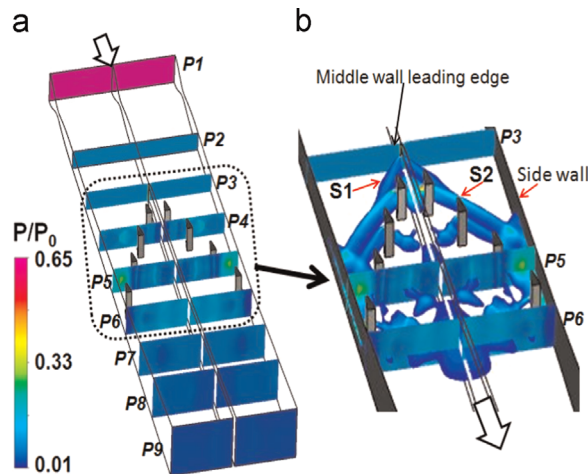

Fig. 7. (a) Pressure distributions at various axial locations and (b) zoomed view to depict three dimensional shock interactions.

wall and struts leading edges, expansion waves are due to struts trailing edge and base [as shown in Fig. 6(a)] and reflection shocks are generated due to side wall of combustor [as seen in Fig. 7(b)]. Static pressure increases on the side wall regions just before the fourth stage struts due to the impingement of the shocks generated from the 2nd and 3rd stage of struts on the wall.

Mass flow average properties of Mach number and total pressure (P_0) loss (TPL) distribution along the length of the combustor are plotted in Fig. 8. Average Mach number is found to reduce from 2.31 at combustor entry to a minimum of 1.4 at $X/h=10.5$, due to shock interaction from middle wall, struts and side wall. In the downstream of the combustor, Mach number increases to ~2.3 at the combustor exit due to flow expansion. The drop of total pressure is more in the fuel injection strut regions at $X/h=4.65–11.63$ ($\Delta P_{0,loss} \sim 53\%$), which is due to the shock interaction from various walls of the combustor. Total pressure loss is about 60% at combustor exit. The ethylene fuel mass fraction ($Y_{C_2H_4}$) at various axial locations is

presented in Fig. 9(a) which shows unmixedness towards the side wall. To elaborate the point, a composite picture of streamline colored with fuel mass fraction and density gradient is plotted in Fig. 9(b) and (c). The fuel streamlines are seen to divert towards combustor core due to complicated shock patterns arising due to leading edge of middle wall, struts and the side wall of the combustor.

The penetration height of fuel is calculated from the distribution of the ethylene fuel streamlines plotted from each injection hole. The penetration of fuel from three injection points (i.e., Points–1, 4, and 9) of strut-1 is shown in Fig. 10. Average penetration height (Z/d_{inj}) adjacent to the injection points is calculated to about 11 (for 9 injection points of strut-1). The penetration height decreases at about 30 injector diameter downstream due to the interaction of the shocks come from other side.

The mixing efficiency (η_m) is defined as the fraction of ethylene mass flux that could be burned (at given state of mixing in case of infinitely fast chemistry) in relation to the total ethylene mass flux and is used to quantify the
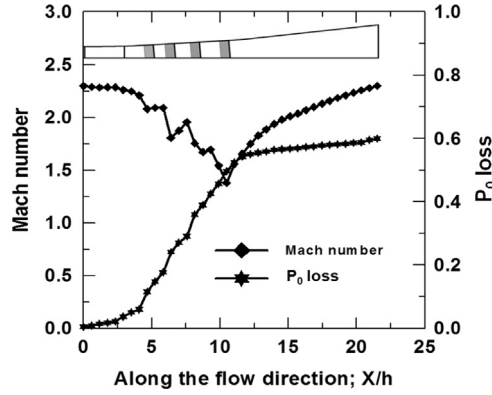
Fig. 8. Axial distribution of mass flow average Mach number and total pressure.
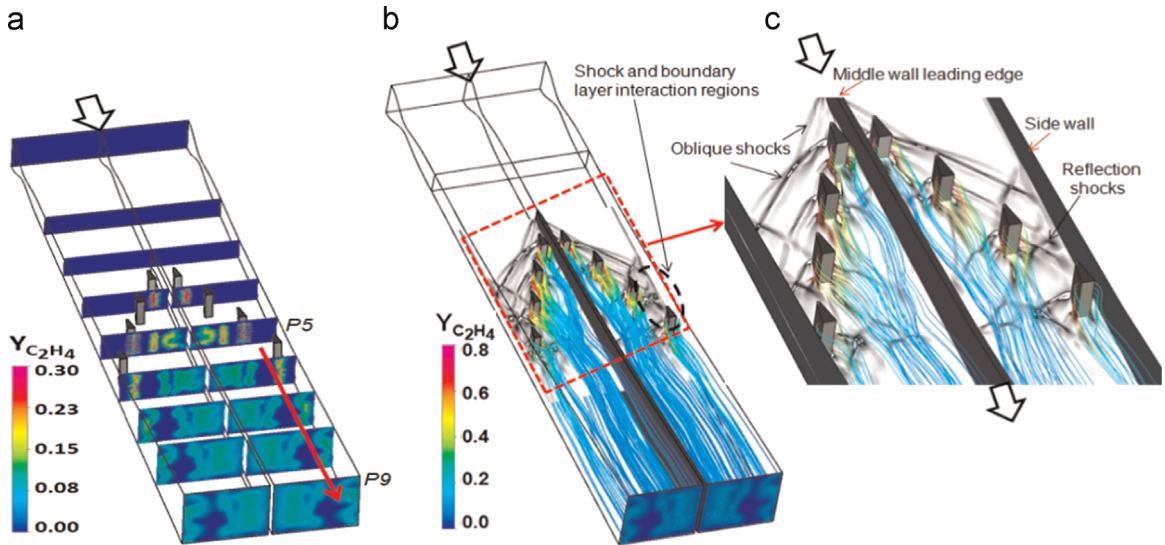

Fig. 9. Ethylene fuel mass fractions (a) various axial location of $Y_{C_2H_4}$, (b) composite picture of streamline color with $Y_{C_2H_4}$ and density gradient and (c) zoomed view at struts regions. (For interpretation of the reference to color in this figure legend, the reader is refered to the web version of this article.)

mixedness of the fuel. The mixing efficiency [25] is evaluated along the combustor flow path as follows:

$$\eta_m(x) = \frac{\int_A \alpha_{gas} Y_{C_2H_4} u dA}{\dot{m}_{C_2H_4}(x)} \qquad (23)$$

With

$$\alpha = \begin{cases} \frac{1}{\varnothing_L}: & \varnothing_L \geq 1, \\ 1: & \varnothing_L < 1 \end{cases}$$

where ρ_{gas} is the gas density, $Y_{C_2H_4}$ is the mass fraction of ethylene, A is the cross-sectional area and u is the axial velocity. Here, $\varnothing_L$ is the local equivalence ratio and is defined as

$$\varnothing_L = 3 * \frac{M_{O_2}}{M_{C_2H_4}} * \frac{Y_{C_2H_4}}{Y_{O_2}}$$

where $M_{C_2H_4}$ and M_{O_2} are the molecular weights of ethylene and oxygen respectively, and Y_{O_2} is the mass fraction of oxygen. Hence $0 < \eta_m < 1$, where $\eta_m = 1$ indicates a perfect

mixing and $\eta_m = 0$ represents complete separation of fuel and oxidizer. The contour of local equivalence ratio ($\varnothing_L$) and mixing efficiency (η_m) at different axial locations along the combustor length is shown in Fig. 11(a) and (b) respectively. The calculated mixing efficiency along the flow direction is shown in Fig. 12. The mixing efficiency is more in the strut regions ($X/h \sim 4.8$–11.3), where fuel is injected, whereas mixing rate is decreased in the downstream of the combustor. The maximum mixing efficiency of about 94% is obtained at the exit of the combustor. Mass flow average values of Mach number, static pressure (P_e/P_0) and temperature (T_e/T_0) at the combustor exit are 1.72, 0.02 and 0.52 respectively.

4.3.2. Simulation of reacting flow

Reacting flow simulations are carried out with transverse injection of ethylene fuel into the main flow through the struts inside the combustor.

4.3.2.1. Grid independance study.
The grid independence of the result is demonstrated by comparing the reacting flow simulation results with two different grids, namely, 4.7 and
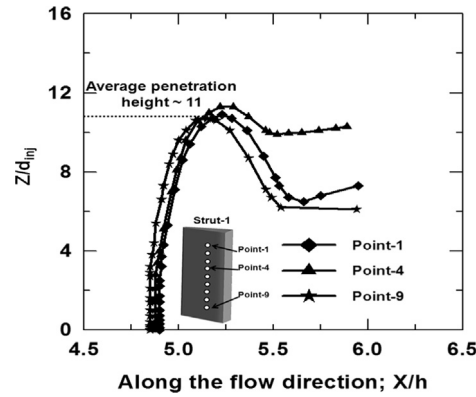
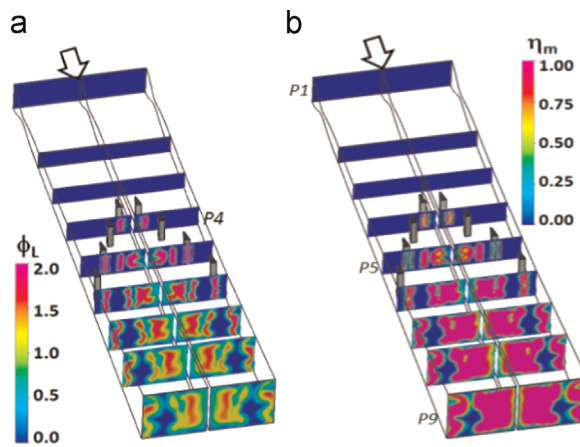**Fig. 10.** Penetration of fuel along the combustor length.

Fig. 11. (a) Local equivalence ratio and (b) mixing efficiency contours at different axial locations.
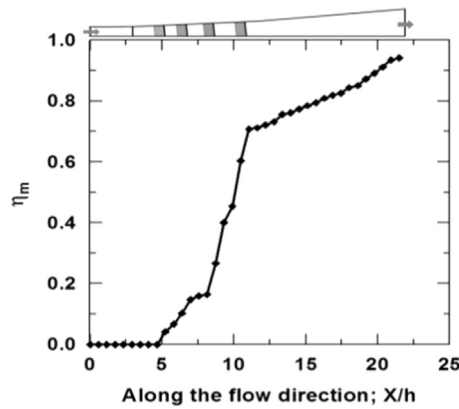

Fig. 12. Mixing efficiency distribution along combustor length.

6.3 million cells. The grids are increased mainly at fuel injection zones, behind the strut and adjacent to the wall regions of the combustor. The top wall surface pressures at $Z/h=1.6$ for two different grids are compared in Fig. 13.

The surface pressures closely match between the coarse and fine grids. An estimate of the error due to grid in the form of Grid Convergence Index (GCI) is also presented in the same figure between the two grids. Roache [26]

proposed a Grid Convergence Index (GCI) as an error based on uncertainty estimate of the numerical solution as
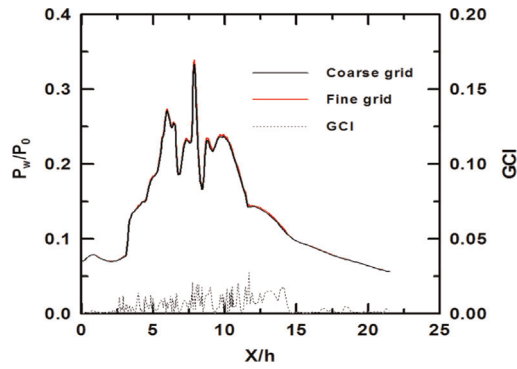
$$GCI = F_s \frac{|\Psi|}{(h_2/h_1)^\epsilon - 1}$$

(24)

Fig. 13. Comparison of top wall surface pressure distribution at $Z/h = 1.6$.
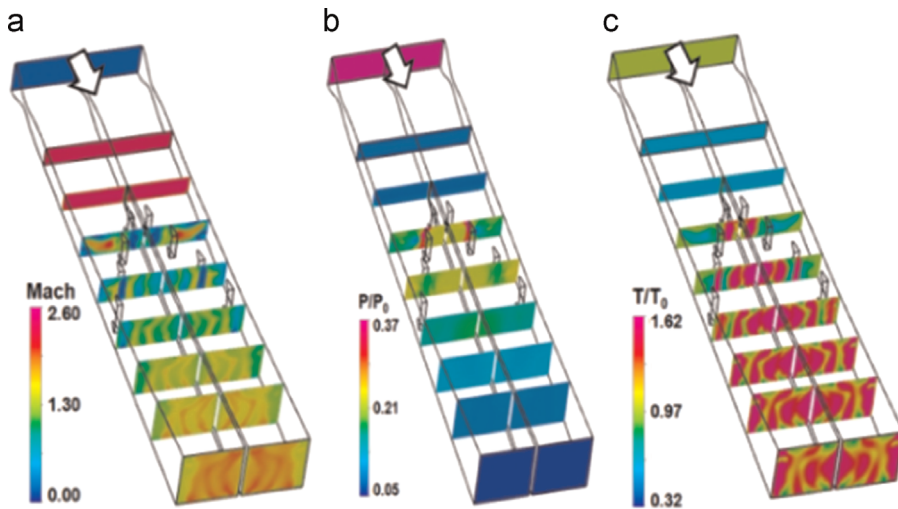

Fig. 14. Contours at different axial locations (a) Mach number, (b) pressure and (c) temperature.
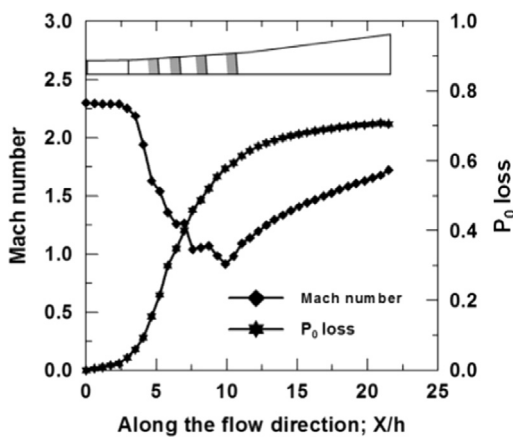

Fig. 15. Axial distribution of average Mach number and total pressure loss.

Here, h is the order of grid spacing, $\in$ is the order of accuracy of numerical scheme and F_s is a factor of safety. Ψ is the relative difference, represented as $\Psi = (f_1 - f_2/f_1)$, where f is any quantity of interest. Suffixes 1 and 2 refer to

the fine and coarse grid solution respectively. In the present calculation, top wall surface pressure has been taken as the parameter of interest. Roache [27] suggested $F_s = 3$ for minimal of two grid calculations. For the present calculation, $\in$ is equal to 2 with h_2/h_1 equal to 2, GCI is order of Ψ. Maximum error between two simulations is within 2.5%. This analysis indicates that the grid is adequate to capture most of features of the flow and the solution is grid independent.

4.3.2.2. Simulation of reacting flow $\phi = 0.72$. Reacting flow simulations are carried out with transverse injection of ethylene fuel into the main flow through the struts with an equivalence ratio of $\phi = 0.72$. Mach number, pressure and temperature distribution at different axial locations are shown in Fig. 14(a)–(c). Mach number is found to decrease while static pressure and temperature increase adjacent to the strut regions due to mixing and combustion of ethylene fuel with vitiated hot air. Significant regions behind the struts are subsonic in contrast to nonreacting flow where Mach number is predominantly supersonic in the whole combustor [Fig. 6(b)]. In the downstream of the
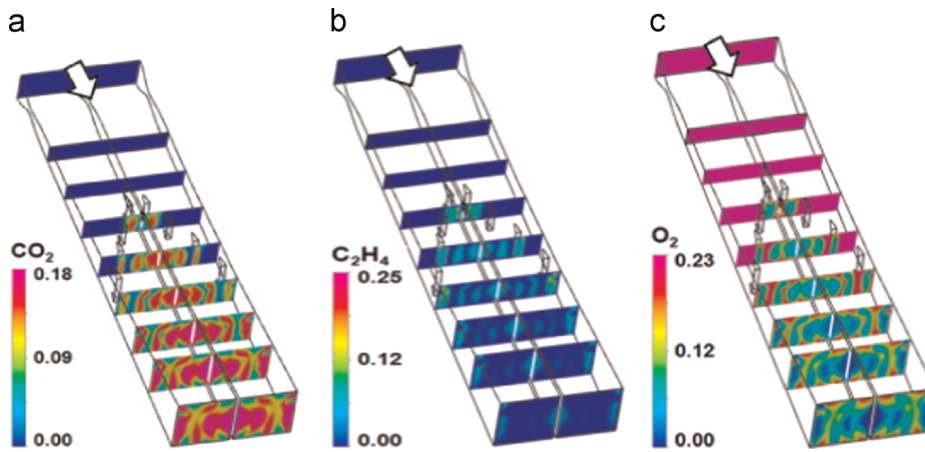
Fig. 16. Species distributions at various axial locations (a) Y_{CO_2}, (b) $Y_{C_2H_4}$, and (c) Y_{O_2}.
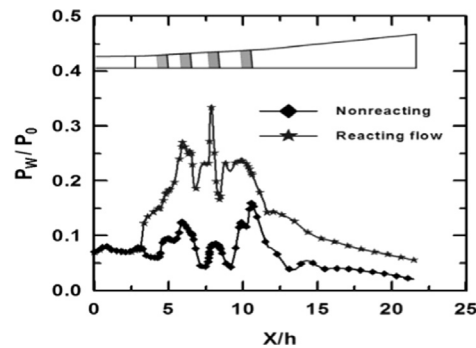

Fig. 17. Axial distribution of wall pressure for reacting and nonreacting flows.

combustor, Mach number starts increasing while pressure and temperature reduce due to expansion of flow.

Mass averaged Mach number and total pressure loss along the length of the combustor are plotted in Fig. 15. Average Mach number is found to reduce from 2.31 at combustor entry to 0.89 at $X/h=9.9$, which is due to shock interaction and combustion of ethylene fuel with vitiated air. In the divergent part of the combustor, Mach number increases to 1.74 at the exit of the combustor. Average Mach number is found to be subsonic in between $9.3 < X/h < 10.1$ of axial length of the combustor. Total pressure availed at the exit of the combustor is 30.3% of the combustor entry value, showing a net P_0 loss of 70% in the whole scramjet combustor which is about 10% more compared to the nonreacting flow condition.

The three dimensional representation of species mass fraction of CO_2, C_2H_4 and O_2 distribution at various axial locations is shown in Fig. 16(a)–(c) respectively. Reaction zones are seen to cover whole width of the combustor from the axial location of $X/h=11.6$ onwards. Small amount of unburnt ethylene fuel is observed adjacent to the side wall and middle wall regions of the combustor [Fig. 16(b)]. Considerable amount of unburnt O_2 [Fig. 16(c)] is found adjacent to the core regions of the combustor due to non-availability of sufficient fuel in these regions.

Computed top wall pressure distributions along the flow direction are shown in Fig. 17 both for nonreacting (with fuel injection) and reacting flow simulations. The

wall pressure (P_w) is nondimensionalised with facility nozzle entry stagnation pressure (P_0). For nonreacting case, pressure rise is mainly due to shock interactions from struts, combustor walls and middle wall leading edges [Fig. 6], while, in case of reacting flow, the pressure rise in the range of $3.5 < X/h < 10$ is mainly due to combustion of ethylene fuel with vitiated air. In the downstream of combustor, pressure reduces continuously due to expansion of flow for both the cases. The calculated nondimensionalised net thrust, $\Delta F/F_{CI}$ [where, ΔF, the difference of the local momentum (F) to the combustor inlet momentum (F_{CI})] and combustion efficiency of the combustor is about 0.265% and 92.0% respectively.

4.3.3. Effect of equivalence ratio (ϕ) on combustor performance

To understand the effect of equivalence ratio (ϕ) on combustor performance, additional 10 more simulations are carried out for different equivalence ratios. Inflow boundary conditions of vitiated air at facility nozzle entry were maintained the same (Table 1) while changing the mass flow rate for fuel by adjusting the fuel total pressure (Table 2). The fuel is injected at sonic condition with stagnation temperature (T_{0_f}) of 300 K.

Computed top wall pressure distributions along the flow direction are shown in Fig. 18 at various equivalence ratio for reacting flow simulations. The wall pressure rises

Table 2
Fuel inflow boundary conditions at different ϕ.

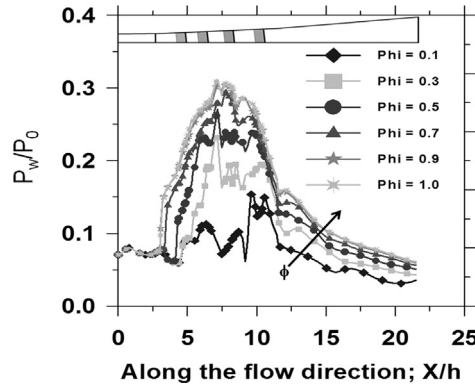| ϕ	0.1	0.2	0.3	0.4	0.5	0.6	0.7	0.8	0.9	1.0
$P_{0_f}/P_{0_{ci}}$	0.50	1.01	1.51	2.01	2.51	3.01	3.51	4.01	4.52	5.02

Fig. 18. Comparison of top wall pressure distribution with different equivalence ratio.

Table 3
Performance parameters of the combustor for different equivalence ratios.

ϕ	$\Delta F/F_{ci}$	η_c	P_0 loss	T/T_0
0.1	0.049	0.995	0.636	0.684
0.2	0.096	0.994	0.651	0.809
0.3	0.142	0.993	0.661	0.915
0.4	0.186	0.987	0.678	1.017
0.5	0.224	0.972	0.681	1.106
0.6	0.253	0.922	0.685	1.172
0.7	0.286	0.906	0.688	1.254
0.8	0.313	0.845	0.691	1.288
0.9	0.326	0.837	0.693	1.337
1.0	0.338	0.768	0.695	1.354

more and more throughout the top wall due to more fuel injected and intense combustion. With increase in the fuel equivalence ratio, the pressure rise location is seen to move upstream.

Thrust is defined as the difference of the momentum between local plane to the inlet of the combustor while combustion efficiency is defined as the ratio of the burnt fuel to the total amount of fuel injected from the struts as follows:

$$\Delta F(x) = \left\lfloor (\dot{m}_a + \dot{m}_{C_2H_4})*u + \int PdA \right\rfloor_x$$
$$- \left\lfloor (\dot{m}_a)*u + \int PdA \right\rfloor_{CI} \qquad (25)$$

$$\eta_c(x) = 1 - \frac{\int_{gas} Y_{C_2H_4} u dA}{\dot{m}_{C_2H_4,\,inj}} \qquad (26)$$

where $\dot{m}_a$, $\dot{m}_{C_2H_4}$ are mass flow rate of vitiated air and fuel respectively.

The net performance of the combustor in terms of thrust, combustion efficiency and maximum total pressure loss (P_0 loss) for different equivalence ratio is tabulated in Table 3. While, the net thrust ($0.05 < \Delta F/F_{ci} < 0.34$) and total pressure loss ($62\% < P_0$ loss $< 69.5\%$) increase with higher equivalence ratio due to more heat release, combustion efficiency (η_c) ($99.6\% > \eta_c > 77\%$) reduces with the increase of ϕ.

5. Conclusions

Numerical simulations of struts based scramjet combustor are carried out to study the mixing and combustion behavior of ethylene fuel and to evaluate combustor performance. Both nonreacting (with fuel injection) and reacting flow are simulated. 3-D RANS equations are solved along with species transport equations and *SST- kω* turbulence model using commercial CFD software CFX-11. Single step chemical reaction is used for combustion of ethylene fuel. Grid independence of the results is demonstrated by performing the simulations with two

different grids and analyzing the Grid Convergence Index (GCI) parameter. Various thermochemical parameters are analyzed to get a better insight of the mixing and combustion process in the combustor. The role of strut leading edge shocks on fuel distribution was examined and the fuel penetration along the length of the combustor is estimated. Maximum pressure rise due to combustion of ethylene fuel with vitiated air is found adjacent to the struts ($3.5 < X/h < 10$). Total pressure loss in reacting flow is observed about 70% in the whole scramjet combustor which is about 10% more compared to the cold flow condition. Effect of equivalence ratio on combustor performance is studied parametrically. With increase of equivalence ratio, top wall pressure increases due to more heat release. Net combustor performance in term of thrust, P_0 loss and efficiency are in the range of $0.05 < \Delta F/F_{ci} < 0.34$, $62 < P_0$ loss $< 69.5\%$ and $99.6 > \eta_c > 77\%$ respectively with the variation of ϕ from 0.1 to 1.0.

Acknowledgments

References

[1] E.T. Curran, S.N.B. Murthy (Eds.), Scramjet Propulsion, Progress in Astronautics and Aeronautics AIAA, Washington, DC, 2001.

[2] C. Gruenig, F. Mayinger, Supersonic combustion of kerosene/H_2-mixtures in a model scramjet combustor, Combust. Sci. Technol. 146 (1999) 1–22.

[3] J. Hu, J. Chang, W. Bao, Q. Yang, J. Wen, Experimental study of a flush wall scramjet combustor equipped with strut/wall fuel injection, Acta Astronaut. 104 (2014) 84–90.

[4] C. Zhang, Q. Yang, J. Chang, J. Tang, W. Bao, Nonlinear characteristics and detection of combustion modes for a hydrocarbon fueled scramjet, Acta Astronaut. 110 (2015) 89–98.

[5] X. Fan, G. Yu, J. Li, L. Yue, X. Zhang, C.J. Sung, Effects of entry conditions on cracked kerosene-fueled supersonic combustor performance, Combust. Sci. Technol. 179 (2007) 2199–2217.

[6] G. Yu, J.G. Li, X.Y. Chang, L.H. Chen, C.J. Sung, Investigation of kerosene combustion characteristics with pilot hydrogen in model supersonic combustors, J. Propuls. Power 17 (6) (2001) 1263–1272.

[7] G. Yu, J.G. Li, X.Y. Chang, X.Y. Chen, C.J. Sung, Fuel injection and flame stabilization in a liquid-kerosene-fueled supersonic combustor, J. Propuls. Power 19 (5) (2003) 885–893.

[8] P. Manna, R. Behera, D. Chakraborty, Design and analysis of liquid fueled strut based scramjet combustor – a CFD approach, J. Propuls. Power 24 (2) (2008) 274–281.

[9] M. Dharavath, P. Manna, D. Chakraborty, Tip to tail simulation of a hypersonic airbreathing cruise vehicle, J. Propuls. Power 31 (5) (2015) 1370–1379.

[10] Z. Zhong, Z. Wang, M. Sun, Effects of fuel cracking on combustion characteristics of a supersonic model combustor, Acta Astronaut. 110 (2015) 1–8.

[11] R.A. Baurle, D.R. Eklund, Analysis of dual-mode hydrocarbon scramjet operation at Mach 4–6.5, J. Propuls. Power 18 (2002) 990–1002.

[12] V. Yang, J. Li, J.Y. Choi, Ignition transient in an ethylene fueled scramjet engine with air throttling, Part I: Non-reacting flow development and mixing, in: Proceedings of the 48th AIAA Aerospace Sciences Meeting Including the New Horizons Forum and Aerospace Exposition, 4–7 January 2010, Orlando, Florida, AIAA 2010-409.

[13] J.C. Doster, P.I. King, M.R. Gruber, Numerical simulation of ethylene injection from in-stream fueling pylons, in: Proceedings of the 15th AIAA International Space Planes and Hypersonic Systems and Technologies Conference 28 April–1 May 2008, Dayton, Ohio, AIAA 2008-2518.

[14] W. Allen, P. King, M. Gruber, Fuel–air injection effects on combustion in cavity-based flameholders in a supersonic flow, in: Proceedings of the 41th AIAA/ASME/SAE/ASEE Joint Propulsion Conference and Exhibit, July 10–13, 2005.

[15] C.J. Tam, K.U. Hsu, M.R. Gruber, Fuel/air mixing characteristics of strut injections for scramjet combustor applications, in: Proceedings of the 26th AIAA Applied Aerodynamics Conference, 18–21 August 2008, Honolulu, Hawaii, AIAA 2008-6925.

[16] S. Pannerselvam, V. Thiagarajan, A.T.K. Ganesh, J.J. Geetha, V. Ramanuchari, Prahlada, Airframe integrated scramjet design and performance analysis, ISABE Paper no. 2005-1280, 2005.

[17] ANSYS-CFX, Release 11.0: Installation and Overview, July 7th 2007.

[18] F.R. Menter, Two-equation eddy-viscosity turbulence models for engineering applications, AIAA J. 32 (1994) 1598–1605.

[19] B.F. Magnussen, B.H. Hjertager, On mathematical modeling of turbulent combustion with special emphasis on soot formation and combustion, in: Proceedings of the Sixteenth Symposium (Int.) on Combustion, The Combustion Institute, 719, 1976.

[20] C.K. Westbrook, F.L. Dryer, Simplified reaction mechanisms for the oxidation of hydrocarbon fuels in flames, Combust. Sci. Technol. 27 (1981) 31–43.

[21] Y. Xiao, W. Song, L. Chen, D. Wang, J. Le, Investigations on ethylene combustion in a scramjet combustor using resistance heaters, Proc. IMechE G - ASME J. Aerosp. Eng. 222 (3) (2008) 411–416, http://dx. doi.org/10.1243/09544100JAERO317.

[22] P. Manna, M. Dharavath, D. Chakraborty, Performance improvement of kerosene fuelled scramjet combustor through modified fuel injection – a CFD study, J. Aerosp. Sci. Technol. 61 (2) (2009) 496–503.

[23] P. Manna, M. Dharavath, P.K. Sinha, D. Chakraborty, Optimization of a flight worthy scram-jet combustor through CFD, Aerosp. Sci. Technol. 27 (2013) 138–146.

[24] ICEM-CFD, Release 11.0: Installation and Overview, July 7th 2007.

[25] M. Dharavath, P. Manna, D. Chakraborty, Thermochemical exploration of hydrogen combustion in generic scramjet combustor, Aerosp. Sci. Technol. 24 (2013) 264–274.

[26] P.J. Roache, Error base for CFD, AIAA Paper no. 2003-0408, 2003.

[27] P.J. Roache, Verification and Validation in Computational Science and Engineering, Hermon Publishers, New Mexico, 1998.